Aperture division multispectral camera for the Earth's reflected solar radiation observation based on the Lagrange L1 point of the Earth-Moon system

HANYUAN ZHANG,[1,2] (iD) XIN YE,[1,*] YUWEI WANG,[1] DUO WU,[1] DONGJUN YANG,[1] AND WEI FANG[1]

[1]*Changchun Institute of Optics, Fine Mechanics and Physics, Chinese Academy of Sciences, Changchun 130033, China*
[2]*University of Chinese Academy of Sciences, Beijing 100049, China*
*yexin@ciomp.ac.cn

Abstract: We propose an aperture division multispectral camera for Earth observation (EAMC) based on the Lagrange L1 point of the Earth-Moon system to measure the Earth's reflected solar radiation (RSR), quantify the effective radiative forcing (ERF) and establish the pixel-scale multispectral angular distribution model (ADM) of the Earth's radiance. The EAMC adopts the snapshot technique to provide multispectral images in the 360-920 nm wavelength, employing nine subsystems sharing a primary system. The camera can capture the entire Earth's two-dimensional morphology and spectral fingerprints at a 10 km spatial resolution, with all spectral images acquired concurrently on a single detector. The camera's optical system is designed and simulated, and the stray light is analyzed and suppressed. Simulation and analysis results show that the camera can obtain high-quality images of the Earth's disk with a 2.5° field of view (FOV). The stray light is suppressed to less than 0.05% of the observed multispectral Earth radiation. The novel EAMC provides a new way to generate climate-relevant knowledge from the perspective of global Earth observation and has great potential for other applications in space-based remote sensing spectral imaging.

1. Introduction

The Earth's radiation budget (ERB) is the radiation exchange process by which the Earth-atmosphere system receives, reflects solar radiation and emits thermal radiation to space [1–3]. Continuous increases in atmospheric greenhouse gas (GHG) concentrations have disrupted the Earth's radiation balance, leading to ongoing global warming [4]. Quantifying this imbalance in the ERB, the Earth Energy Imbalance (EEI), is critical to understanding our current and future ecological environment.

Effective radiative forcing (ERF) is essential for EEI quantification. A fundamental question motivating the sixth phase of the Coupled Model Intercomparison Project (CMIP6) [5] is: "How does the Earth system respond to forcing?" The answer to this question depends on accurately characterizing the ERF in the reflected solar radiation (RSR), which is also an essential objective for measuring the EEI in space [6,7]. The Sixth Assessment Report of the Intergovernmental Panel on Climate Change (IPCC AR6) shows that the influential radiative forcing factors mainly include clouds, aerosols, greenhouse gases, surface albedo, and land use efficiency [8]. It also emphasizes that the cloud ERF is a primary source of uncertainty in current transient warming projections [9]. Furthermore, the angular distribution model (ADM) is another critical factor in EEI inversion [10]. Since ERB detectors typically measure the radiant flux, this should be converted to irradiance or radiance utilizing an ADM, which depends not only on the viewing

geometry but also on the cloud conditions and the surface type beneath the area at the TOA. Scene radiance ADMs are therefore required.

To date, the most widely used ERB data are supplied by the Clouds and Earth Radiation Energy System (CERES) [11]. The CERES combines multispectral radiance data from MODIS to provide albedo, cloud, and other ERFs from different surface scenes and performs regional elevation and azimuth scans to collect anisotropy radiance for the construction of today's ADM [12,13]. The Changchun Institute of Optics, Precision Mechanics and Physics, Chinese Academy of Sciences proposed a new instrument concept for measuring ERB at the TOA. Instead of regional scans, a non-scanning radiometer will measure the integrated Earth radiation in wavelengths of 0.2-5.0 μm and 0.2-50.0 μm at the Earth-Moon system's Lagrange point L1, which has entered prototype performance testing. [14]. This radiometer's main innovation is removing the error in linking multiple regional ERB data time series to the integral ERB computations and acquiring global radiation in hours. However, due to the instrument's work mechanism, there was an urgent need to characterize the ERFs and establish the ADMs under the radiometer's observing geometry. Therefore, a shortwave (360-920 nm) aperture division multispectral camera for Earth observation (EAMC) will be supplemented to identify the scene and provide ERF information by measuring RSR. As the Earth is observed globally at the L1 point, different scenes will be imaged on different detector pixels with changing radiance and geometry as the Earth rotates. Thus, the EAMC will also attempt to provide the necessary data for a new multispectral ADM and work in conjunction with the radiometer to deliver more accurate RSR observations.

Numerous multispectral imaging methods have been proposed in the past. But for imaging the entire Earth while receiving spectral radiation at the L1 point, using scanning techniques such as push-broom [15] to obtain the surface "three-dimensional data cube" composed of two-dimensional morphology and spectral fingerprints is unsuitable. Moreover, using a filter wheel or a liquid crystal tunable filter system [16] for time-sharing measurements risks losing information about transient changes in Earth's radiation across seasons and latitudes during operation. For this reason, we propose an aperture division multispectral camera inspired by the optics of the compound eye, which can concurrently acquire nine global spectral images of the Earth on a single image sensor, with each spectral channel having a spatial resolution of 10 km. The EAMC is a snapshot spectral imaging system [17,18] that can simultaneously collect the Earth disk's global spatial and spectral information, improve the timeliness of ERF data, and support the establishment of a pixel-scale multispectral ADM.

This manuscript focuses on the optical design and stray light control of the EAMC. In Section 2, we establish the energy distribution relationship between the object and the image of the EAMC and describe the instrument's requirements and conceptual design. The performance of the optical system is presented in section 3. Section 4 describes the tolerance error budget of the camera. Section 5 describes the stray light suppression and analysis. A discussion of the results is given in section 6. Section 7 presents conclusions on the optical design and stray light control for the EAMC system.

2. EAMC optical system design

2.1. Technical constraints and configuration

According to the main application of the camera, the system's requirements can be clearly defined. (1) The camera's field of view (FOV) should cover the whole Earth at the Lagrange point L1 of the Earth-Moon system. (2) The ability to identify the scene and quantify the corresponding RSR values. (3) A resolution of 10 km to distinguish between cloudy and clear-sky scenes [19]. (4) Capable of rapidly imaging the Earth to avoid loss of climate change information during operation. (5) Clear imaging and provision of regional scene radiation within the spectral bands of 360-380 nm, 430-450 nm, 460-480 nm, 490-530 nm, 540-560 nm, 620-670 nm, 740-750 nm, 850-880 nm and 890-920 nm.

As shown in Fig. 1, the EAMC essentially consists of a data processing unit with an image sensor, a front primary system, and nine rear aperture subsystems with various bandpass filters. The aperture stops are located on the first surface of the subsystems. The EAMC has nine spectral channels arranged in three rows and three columns. Each subsystem forms a spectral channel with the primary system. Solar radiation reflected from the Earth enters the system, converges through the primary system, and is then split by the subsystems into nine focused beams. Because the nine subsystems share a single detector, they can simultaneously observe the same uniform light source during ground tests to compare detector sensitivity differences between channels. The wavelengths of the nine channels for scene identification and observation of clouds, snow, plants, oceans, deserts, and water vapor are 360-380 nm, 430-450 nm, 460-480 nm, 490-530 nm, 540-560 nm, 620-670 nm, 740-750 nm, 850-880 nm, and 890-920 nm, respectively. Subsystem efficiencies at different wavelengths will be pre-tested in the laboratory. This could also be determined in orbit by observing the entire lunar disc for cross-calibration. As a note, current aperture division optical systems focus on achieving a large FOV and high spatial resolution using lower-resolution images from multiple separate FOVs for super-resolution reconstruction [20,21]. However, as well as imaging the Earth spectrally, our EAMC is also a data source for the ADM and ERF. Each pixel of each spectral image must have a specific geometric relationship to the corresponding ground object and a numerical relationship to the corresponding spectral fluxes to analyze the radiance anisotropy of the scenes, which is struggling to achieve with segmented FOV observation and high-resolution image reconstruction. Therefore, the spatial resolution of each EAMC channel is set to 10 km. The EAMC has several observation and calibration modes. In addition to the normal single radiation measurements, a repeated snapshot mode can be selected for certain weak radiation scenes to improve the signal-to-noise ratio. In-orbit calibration modes using a solar diffuser and the Moon will also be provided to monitor the responsivity of the EAMC after absolute radiometric calibration in the laboratory.
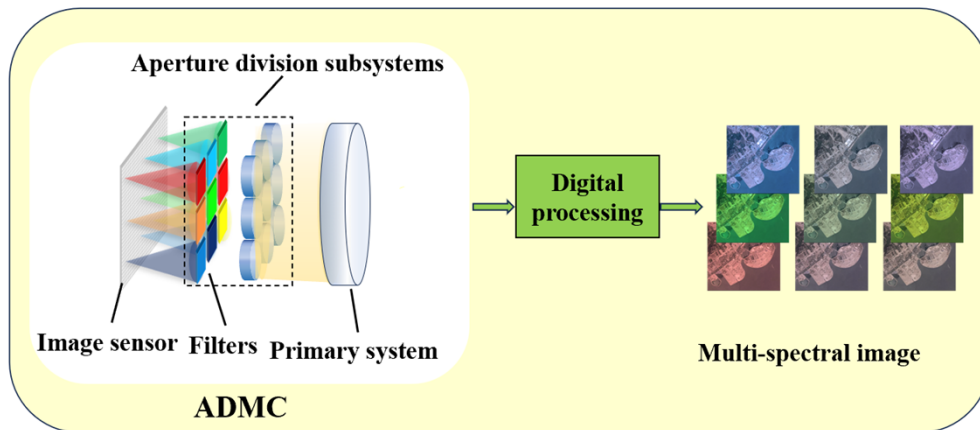
Fig. 1. Schematic diagram of EAMC system composition.

Figure 2 shows the observation geometry of the EAMC. The FOV of the EAMC can be defined by Eq. (1) based on the spatial observation position and the target.
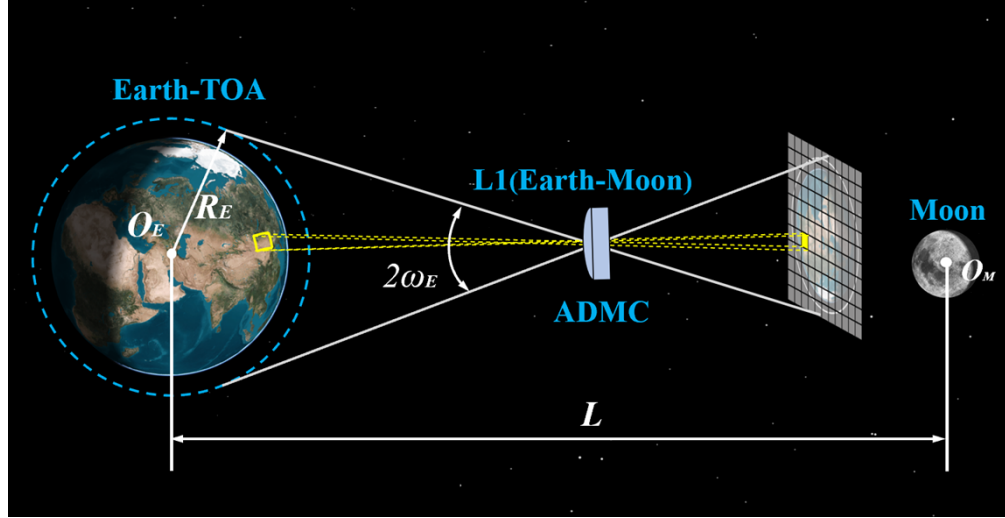
$$\sin \omega_E = \frac{R_E}{\rho} \tag{1}$$

where ω_E is half the FOV angle for observation of the Earth's hemisphere at point L1, R_E is the Earth's radius, $R_E = 6371$ km, and ρ is the distance between the Earth's centroid and point L1. ρ

can be expressed as:

$$\rho = 0.85L \tag{2}$$

where L is the average Earth-Moon distance, L = 384403.9 km.

Fig. 2. The EAMC space observation schematic diagram includes crucial geometric parameters. The origin of the Earth and the Moon are demarcated by O_E and O_M.

We favor using a plane array monochromatic CCD comprising 10560×10560 pixels of 9 μm as the image sensor for the EAMC, which can be photosensitive in the range of 300 to 1000 nm [22]. The focal length of the camera f_c can be defined as Eq. (3) based on the spatial resolution requirements and the principles of geometry.

$$\frac{G}{f_c} = \frac{D_d}{L} \tag{3}$$

where G is the desired size of each pixel corresponding to the ground object, $G = 10$ km, and d is the pixel diameter of the detector, $D_d = 9$ μm.

Due to the need to create nine images on the detector, the image area of each spectral channel should be divided, i.e., Eq. (4) should be satisfied to ensure imaging requirements.

$$h \le \frac{N \cdot D_d}{M} \tag{4}$$

where h is the image height of each spectral channel; N is the resolution of the detector, $N = 10560$; and M is the number of rows or columns of the subsystem, $M = 3$.

2.2. Principle

This section illustrates the light intensity distribution relationship between the object and the image of the aperture division optics [23,24]. In Fourier optics, the optical system can be regarded as a linear time-invariant system, and the image intensity distribution obtained on the detector $g(x, y)$ is the convolution of the object intensity $f(x, y)$ and the intensity point spread function (PSF) of the system $PSF(x, y)$, which can be described as Eq. (5).

$$g(x, y) = f(x, y) * PSF(x, y) \tag{5}$$

Understanding the imaging characteristics of an optical system requires the determination of its PSF, which is the modular square of the Fourier-transformed pupil function in a diffraction-limited

system with incoherent illumination. Figure 3 shows a schematic diagram of an aperture division optical system with an eccentric distance in each channel except the central channel. A typical optical imaging system for the central channel comprises rear and front lens lenses. Since the exit pupil is circular, the corresponding pupil function $p_c(x, y)$ is a circular domain function, which can be expressed as:

$$p_c(x, y) = circle\left(\frac{\sqrt{x^2 + y^2}}{D/2}\right) \tag{6}$$

where x and y respectively denote the coordinates in the lens aperture of the central channel.
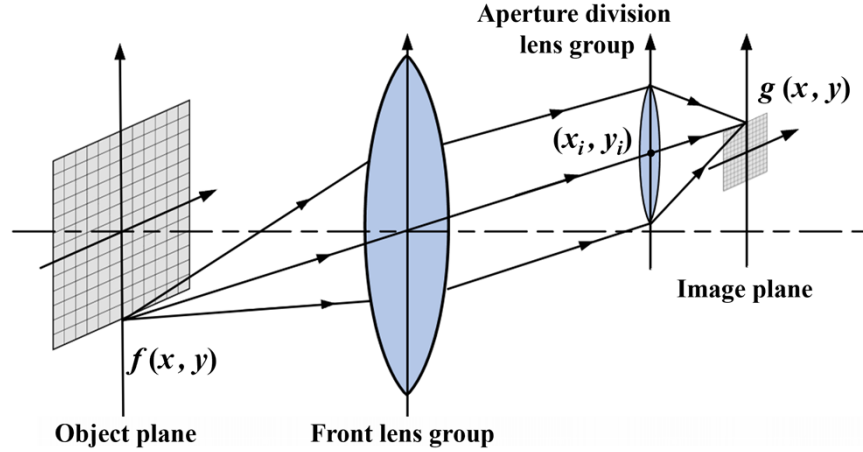

Fig. 3. The image-object relationship for the aperture division optics.

The PSF that corresponds to the typical circular aperture $PSF_c(x, y)$ can be written as:

$$PSF_c(x, y) = \left(\frac{\pi D^2}{4\lambda f}\right)^2 \left[\frac{2J_1(\frac{\pi D\sqrt{x^2+y^2}}{\lambda f})}{(\frac{\pi D\sqrt{x^2+y^2}}{\lambda f})}\right] \tag{7}$$

where J_1 is the first-order Bessel function, D is the diameter of the exit pupil, λ is the working wavelength of the system, and f is the focal length of the system.

For the other channels with an eccentric distance, the pupil function $p_e(x, y)$ is represented as follows:

$$p_e(x, y) = circle\left(\frac{\sqrt{x^2 + y^2}}{D/2}\right) * \delta(x - x_i, y - y_i) \tag{8}$$

where x_i and y_i respectively denote the central coordinates in the lens aperture of the eccentric channel.

Therefore, the PSF of the eccentric channel $PSF_e(x, y)$ is given by:

$$PSF_e(x, y) = F\{p_e(x, y) \otimes p_c(x, y)\}$$

$$= \left(\frac{\pi D^2}{4\lambda f}\right)^2 \cdot \left(\frac{2J_1(\frac{\pi D\sqrt{x^2+y^2}}{\lambda f})}{(\frac{\pi D\sqrt{x^2+y^2}}{\lambda f})}\right) \cdot \left|\exp[-\frac{j2\pi}{\lambda f}(xx_i + yy_i)]\right|^2 \tag{9}$$

The intensity distribution relationship between the object and the image has now been established. Based on the above imaging principles, a suitable eccentric distance must be specified to avoid overlapping the apertures, which can also modulate the images.

2.3. Optical design of the EAMC

Based on the above principles and application requirements, the EAMC is designed with the following characteristic parameters, as shown in Table 1.

Table 1. EAMC optical design parameters

Parameter	Specification
Field of view (FOV)	±1.25°
Effective focal length (EFL)	341.9mm
F-number	6.3
Wavelength	360-380 nm, 430-450 nm, 460-480 nm, 490-530 nm, 540-560 nm, 620-670 nm, 740-750 nm, 850-880 nm, 890-920nm

Figure 4(a) shows the 3D optical layout in ZEMAX for the designed EAMC. As can be seen, there are nine spectral channels, i.e., a subsystem integrated with selected narrowband optical filters, a primary system, and an image sensor. Each channel contains six achromatic doublets to eliminate chromatic aberrations. A flat glass plate ($d = 3$ mm) with a specific transmission wavelength and refractive index, whose data were taken from the SCHOTT glass catalog in ZEMAX, was used to simulate the optical filter between each subsystem and the image sensor. Figure 4(b) illustrates the positions of the different spectral channels, and Table 2 shows the eccentric distance of each channel. The eccentric distance is defined as the deviation in distance between the optical axes of the nine subsystems and the central axis of the primary system along the x- or y-axis direction, which determines the subsystems' spatial distribution. After multiple optimizations and adjustments, the nine channels are regularly arranged in three rows and columns. The off-center distance of the eccentric channels from the central channel along the x- or y-axis direction is 40 mm.
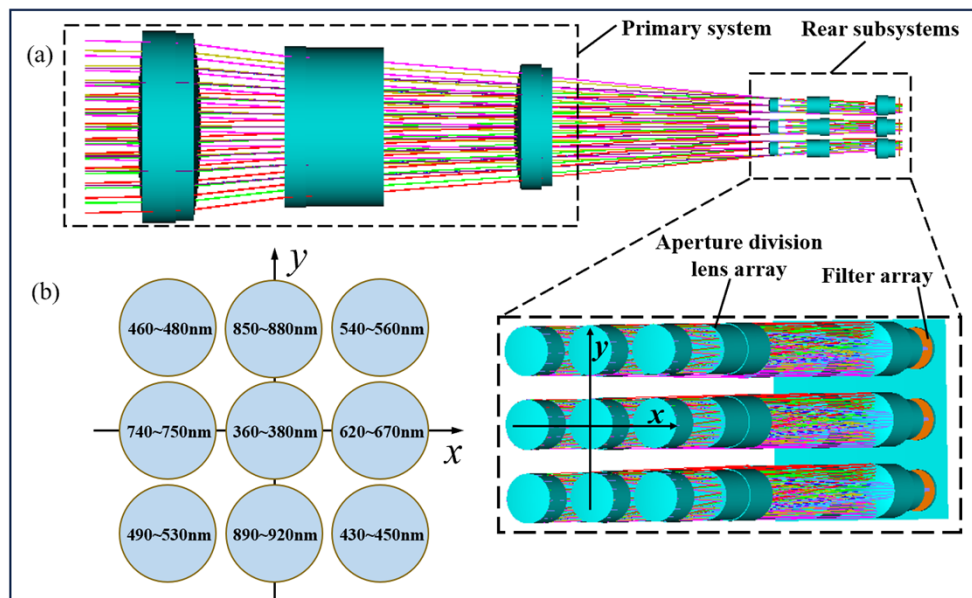
Fig. 4. The EAMC system. (a) 3D layout for the EAMC with a local enlarged drawing of nine subsystems. (b) Explanatory drawing of nine spectral channels' position.

Table 2. Eccentric distance of the nine subsystems.

Spectral channel	X-axis eccentric distance	Y-axis eccentric distance
360-380nm	0	0
430-450nm	40mm	-40mm
460-480nm	-40mm	40mm
490-530nm	-40mm	-40mm
540-560nm	40mm	40mm
620-670nm	40mm	0
740-750nm	-40mm	0
850-880nm	0	40mm
890-920nm	0	-40mm

Table 3. Lens data: surface curvatures, semi-diameters, thickness, and materials. The first six lenses form the primary system, and the last six form a subsystem. Each subsystem's lens parameters are the same.

	Front surface curvature	Back surface curvature	Semi-diameter	Thickness	Material
1_{st} lens	1722.826mm	718.707mm	157.439mm	50.944mm	LAKN7
2_{nd} lens	718.707mm	-997.873mm	154.702mm	66.657mm	N-PK51
3_{rd} lens	-2548.203mm	-237.647mm	131.274mm	76.451mm	P-SK57
4_{th} lens	-237.647mm	5569.895mm	128.081mm	101.107mm	N-KZFS4
5_{th} lens	510.659mm	251.740mm	99.451mm	27.483mm	K7HT
6_{th} lens	251.740mm	457.546mm	95.323mm	32.264mm	F13
7_{th} lens	103.589mm	81.015mm	13.234mm	9.437mm	N-LAK21
8_{th} lens	81.015mm	231.964mm	13.165mm	7.230mm	SSKN8
9_{th} lens	-375.451mm	17.537mm	14.561mm	18.016mm	N-SSK2
10_{th} lens	17.537mm	-169.149mm	15.357mm	24.991mm	N-PSK57
11_{th} lens	43.526mm	21.319mm	18.023mm	18.034mm	BASF13
12_{th} lens	21.319mm	17.625mm	14.776mm	17.625mm	K5HT

Table 3 shows the EAMC lens parameters. As the camera requires imaging in the ultraviolet-near infrared spectral range, the lens material must be capable of transmitting radiation in 360-920 nm. Furthermore, the most critical aspect of multispectral imaging is chromatic aberration elimination, which depends on the choice of optical materials. The materials are continuously simulated with different groups to approach the diffraction limit, and the optimal solution is finally obtained by hammer and global optimization in ZEMAX. During the design process, the primary and subsystems are optimized separately, and then both are optimized together following pupil matching. The F-number must be the same for the primary and subsystems. Once the eccentric distance of the subsystems is determined, their spatial distribution can be used as a reference for the parameters of the primary system, so we choose to design the subsystems first. Since one single detector should receive all the spectral images, the eccentric distance should be kept under reasonable control. Otherwise, a sensor might not be able to obtain all nine pictures, or the apertures of the subsystems might overlap. After simulating the combination of the subsystems with the primary system, the focal length of the entire system is set to a constant 341.9 mm, and the nine subsystems are developed into nine configurations that are jointly optimized in ZEMAX. In multi-configuration co-optimization, it is imperative to minimize inter-channel chromatic aberration to avoid inconsistent optimal axial positions of image planes between channels in parallel with single-channel chromatic aberration. In addition,

the curvature and thickness of the lens in the nine channels are fixed at the same value to avoid difficulties during mechanical assembly. Optimization of the optical design is aimed at matching the spot size to the Airy disc to achieve a near-diffraction-limited optical system.

3. Optical performance

The modulation transfer function (MTF) is a vital parameter for evaluating the imaging quality of optical systems. Figures 5(a)–5(i) show the MTF curves of the nine channels at different wavelengths in the EAMC. In Fig. 5, the lines in different colors correspond to the fields between -1.25° and +1.25°.

$$N = \frac{1000}{2D_d} \tag{10}$$

It can be seen that at the Nyquist frequency of 55 cycles/mm (calculated using Eq. (10) [25]), the 360-380 nm channel has the highest MTF value of 0.81, while the 890-920 nm channel has the lowest MTF value of 0.57, and the curves are flat, indicating that the EAMC images have good uniformity and spatial contrast ratio throughout the whole FOV.

We further consider the spot diagram, which assesses the performance of the EAMC. The spot size is simulated for different fields between -1.25° and +1.25°. In the simulation, each channel's maximum, minimum, and center wavelengths are input, with different colors representing
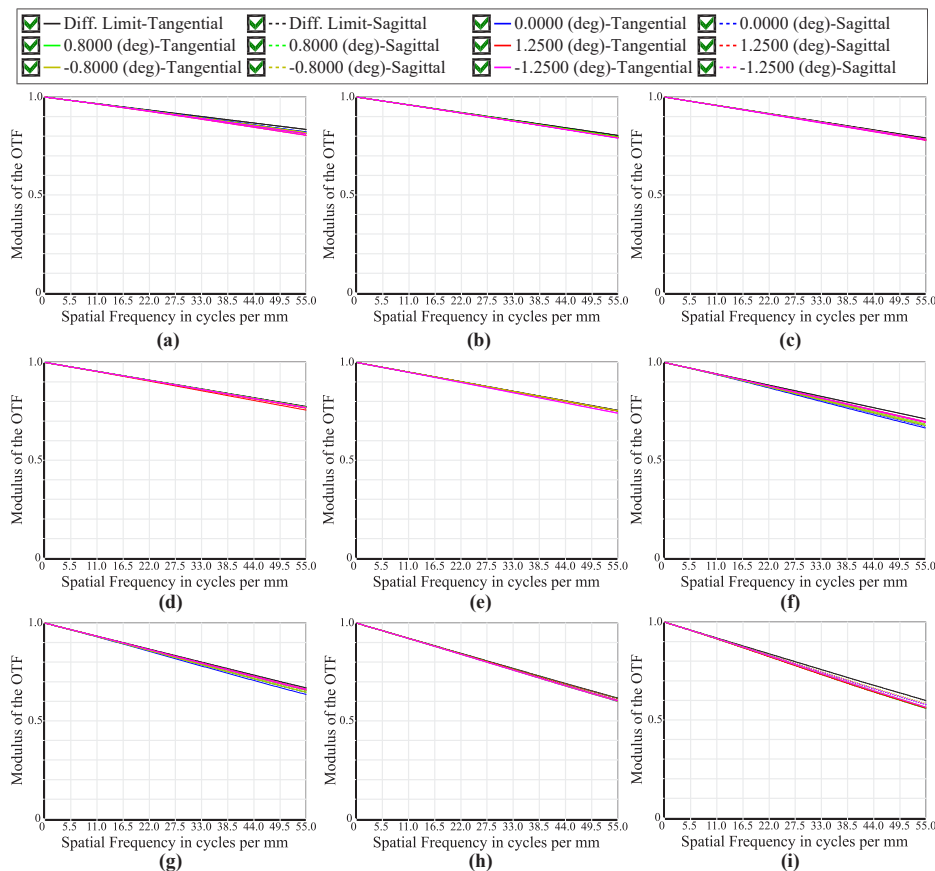
Fig. 5. The MTF for different channels at the fields between -1.25° and 1.25°. (a) 360-380 nm, (b) 430-450 nm, (c) 460-480 nm, (d) 490-530 nm, (e) 540-560 nm, (f) 620-670 nm, (g) 740-750 nm, (h) 850-880 nm, (i) 890-920 nm.
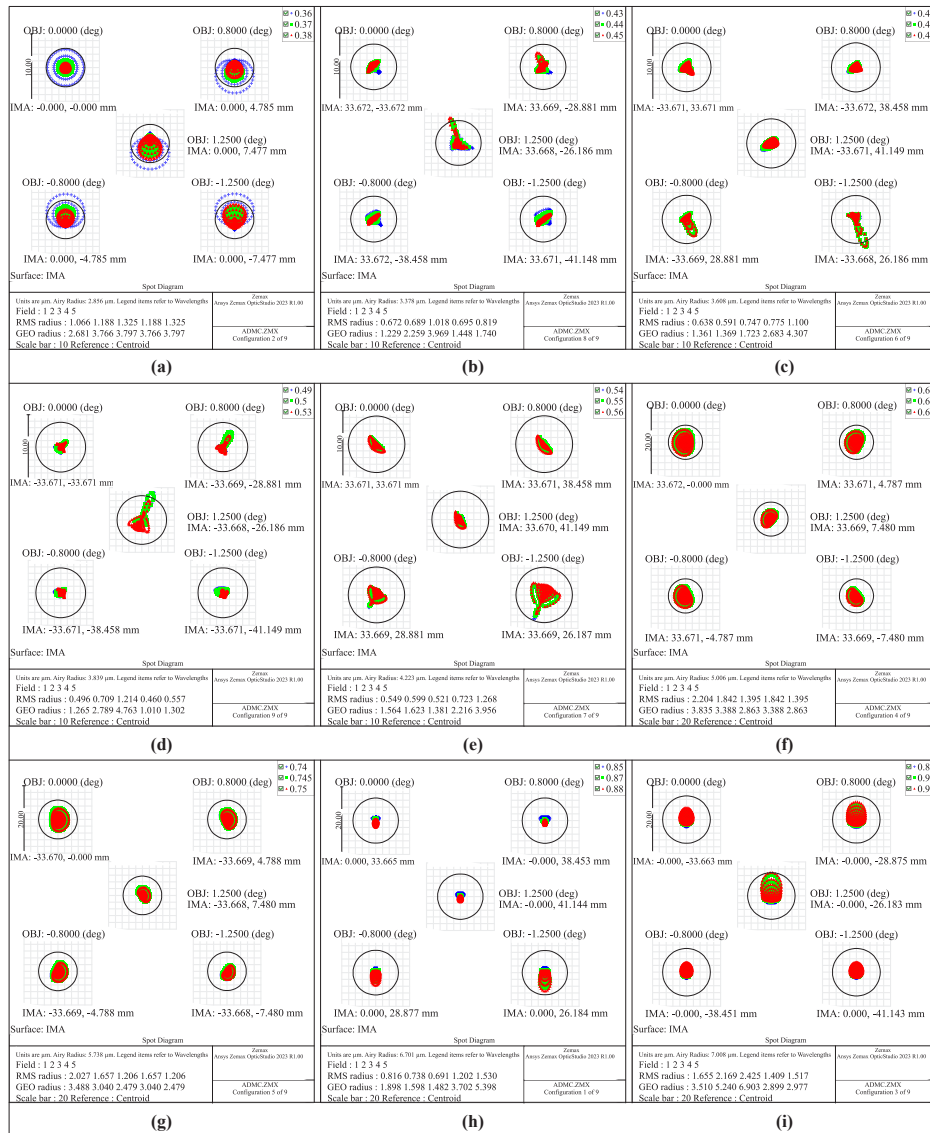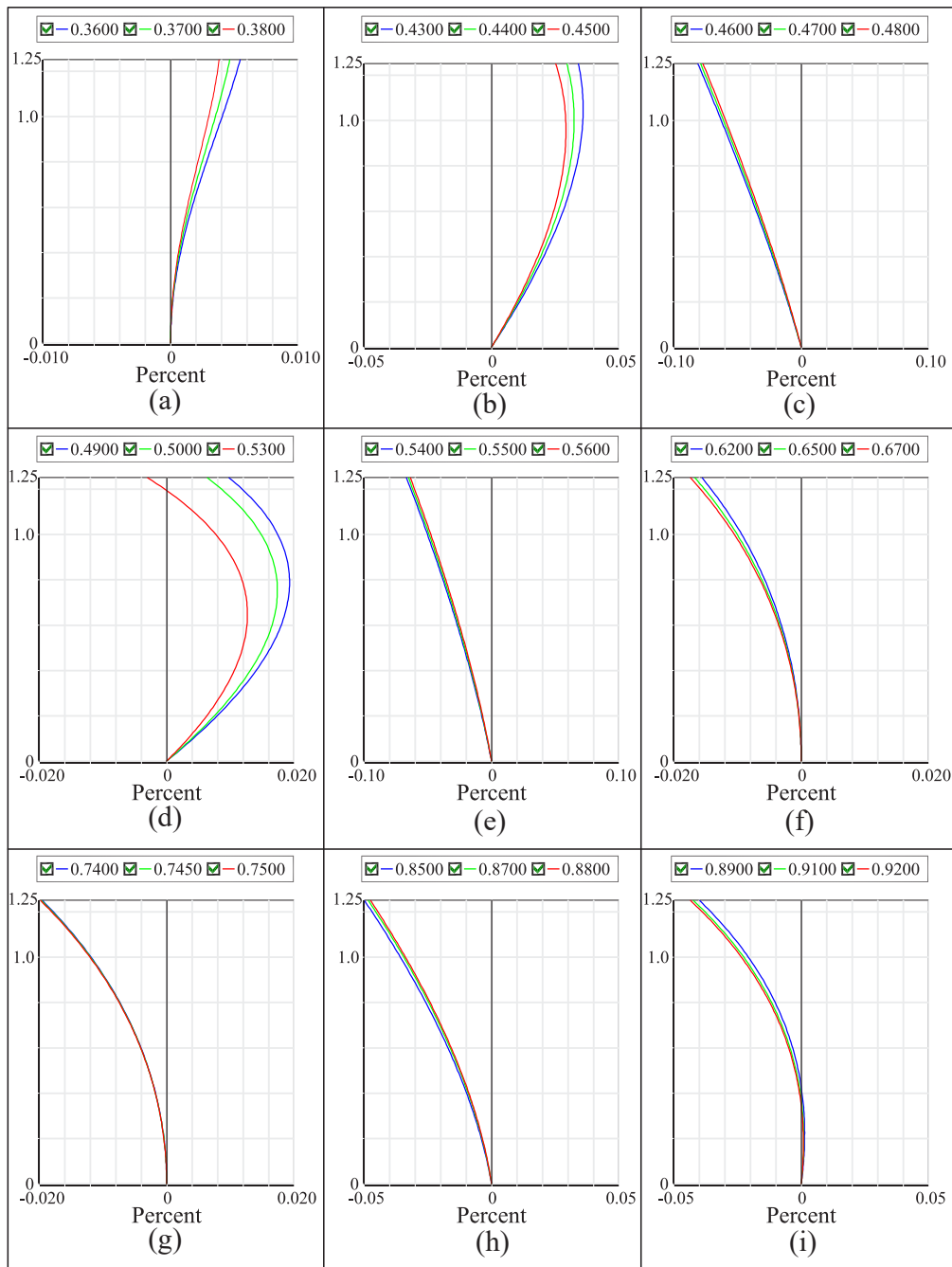
Fig. 6. The Spot diagram for different channels at the fields between -1.25° and 1.25°. (a) 360-380 nm, (b) 430-450 nm, (c) 460-480 nm, (d) 490-530 nm, (e) 540-560 nm, (f) 620-670 nm, (g) 740-750 nm, (h) 850-880 nm, (i) 890-920 nm. OBJ (in degrees) defines the object field, and IMA (in mm) specifies the image height of the centroid on the detector.

different wavelengths in Figs. 6(a)–6(i) and the black circles corresponding to the Airy disks. The root-mean-square (RMS) radius of the spot is calculated by using the gravity center as a reference through the randomly incident light. As shown in Figs. 6(a)–6(i), all the RMS radii of the nine channels in different FOVs are smaller than the Airy disks and one pixel. Simulations based on the optimized lens material allocation and geometric parameters make known that the optical system has good imaging capability in 360-920 nm. The longitudinal and lateral chromatic aberrations are well eliminated, and the resolutions are close to the diffraction limit.

The MTF and spot diagram cannot fully describe the imaging performance of optical systems as they do not have a visual representation of the distortion, which is a deformation between the
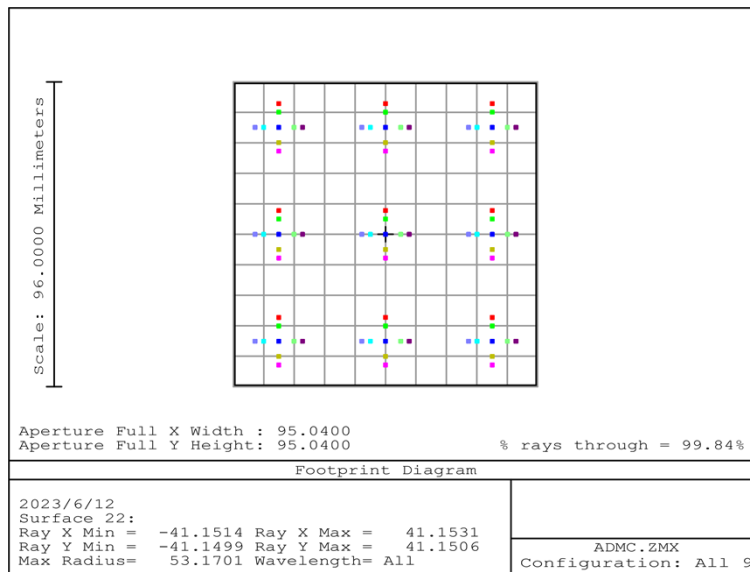
Fig. 7. The distortion curves for different channels at the fields between 0° and 1.25°, in which the horizontal axis expresses the distortion in %, and the vertical axis gives the half FOV. (a) 360-380 nm, (b) 430-450 nm, (c) 460-480 nm, (d) 490-530 nm, (e) 540-560 nm, (f) 620-670 nm, (g) 740-750 nm, (h) 850-880 nm, (i) 890-920 nm.
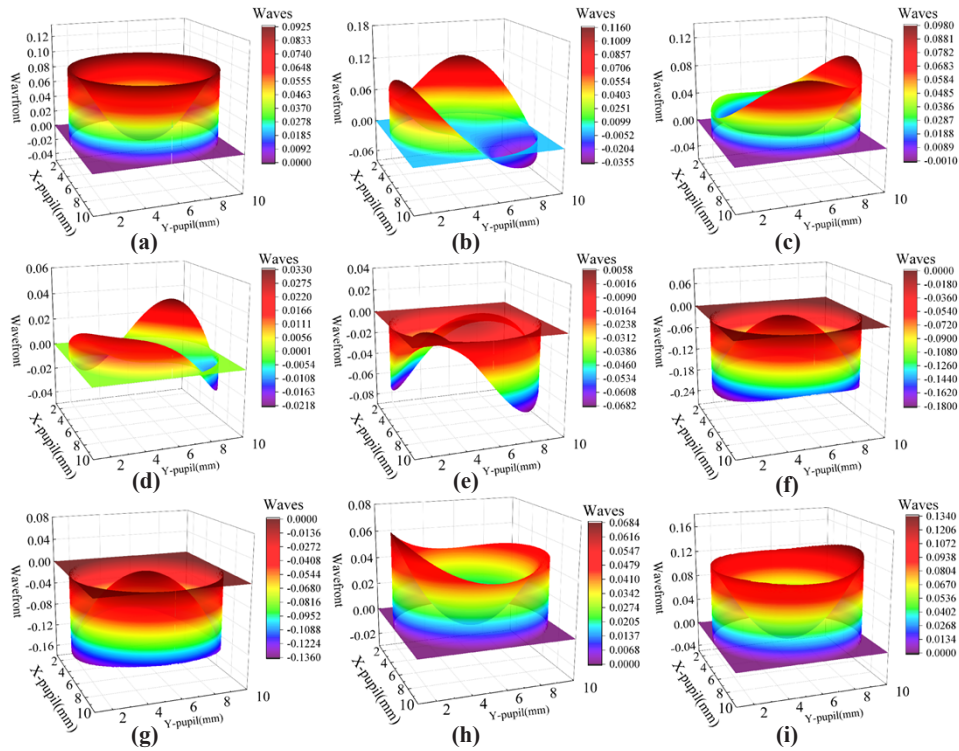
Fig. 8. The wavefront maps for different channels at 1.25°, in which the x and y axis represent the coordinate positions of the pupil. (a) 360-380 nm, (b) 430-450 nm, (c) 460-480 nm, (d) 490-530 nm, (e) 540-560 nm, (f) 620-670 nm, (g) 740-750 nm, (h) 850-880 nm, (i) 890-920 nm.

Fig. 9. Footprint diagram of the EAMC.

actual and ideal images. Therefore, the distortion curves of nine channels at the maximum FOV, with different colors representing different wavelengths, are shown in Figs. 7(a)–7(i). Statistically, the 460-480 nm channel has the maximum distortion (in %) at 1.25°, which equals 0.1137%, causing a minor change in image height of less than one pixel.

The wavefront aberrations must also be examined to verify the imaging quality of the EAMC with high imaging requirements and low geometric aberrations. Figures 8(a)–8(i) show the EAMC's wavefront maps at a maximum FOV of 1.25°. Figure 8 shows that the 620-670 nm channel has the maximum wavefront peak-to-valley (PV) value of 0.18λ and less than $\lambda/4$, implying that the quality of the actual optical system is not significantly different from that of the ideal optics as per the Rayleigh criterion [26].

The ability to capture the nine images on one detector is important. Figure 9 shows the nine-channel footprint diagram of the EAMC, which shows that the image sensor can receive all the pictures within a detection area of 95.04×95.04 mm (the same as the photosensitive area of the CCD) without any crosstalk or loss.

4. Tolerance analysis for EAMC

Tolerance analysis is indispensable to meet the requirements of practical machining and is therefore carried out in this section. We used the sensitivity and Monte Carlo analysis methods with the MTF better than 0.5 and the RMS wavefront less than 0.06λ as the desired evaluation criteria. An adopted allocation of the tolerances obtained from the sensitivity analysis is shown in Table 4, from relatively loose initial values through several iterative tightenings to ensure the optical performance of the EAMC. These tolerances are specified separately for the nine channels, as the image quality of each channel is affected to a varying degree by different tolerances. As can be seen from the table, each channel is most sensitive to the decenter and tilt of the lens surface, so these two tolerances are the most restrictive of all.

Table 4. Specifications of the tolerance allocation scheme

Parameter	Specification								
Spectral range/nm	360-380	430-450	460-480	490-530	540-560	620-670	740-750	850-880	890-920
The radius of curvature tolerance/mm	±0.02	±0.01	±0.01	±0.02	±0.04	±0.01	±0.01	±0.04	±0.02
Thickness tolerance/mm	±0.02	±0.01	±0.01	±0.02	±0.04	±0.01	±0.01	±0.04	±0.02
Eccentric distance of lens surface(mm)	±0.01	±0.005	±0.005	±0.01	±0.02	±0.005	±0.005	±0.02	±0.01
Inclination of lens surface(°)	±0.01	±0.005	±0.005	±0.01	±0.02	±0.005	±0.005	±0.02	±0.01
Inclination of lens element(°)	±0.02	±0.01	±0.01	±0.02	±0.04	±0.01	±0.01	±0.04	±0.02
Refractive index tolerance	±0.001	±0.001	±0.001	±0.001	±0.001	±0.001	±0.001	±0.001	±0.001
Abbe number tolerance/%	±1	±1	±1	±1	±1	±1	±1	±1	±1

Figure 10 shows the EAMC's cumulative probability curves of the MTF and RMS wavefront, generated after randomly sampling one thousand lens groups using the Monte Carlo method. The plots illustrate an overwhelming 97% probability that the MTF is higher than 0.5 and the RMS wavefront is less than 0.06λ. According to the figures, the most significant change is that the MTF of the 890-920 nm channel drops by 0.2 to 0.55, and the RMS of the 430-450 nm, 620-670 nm, and 890-920 nm channels are 0.053λ, demonstrating that the tolerance allocation is rational for manufacturing and assembly.
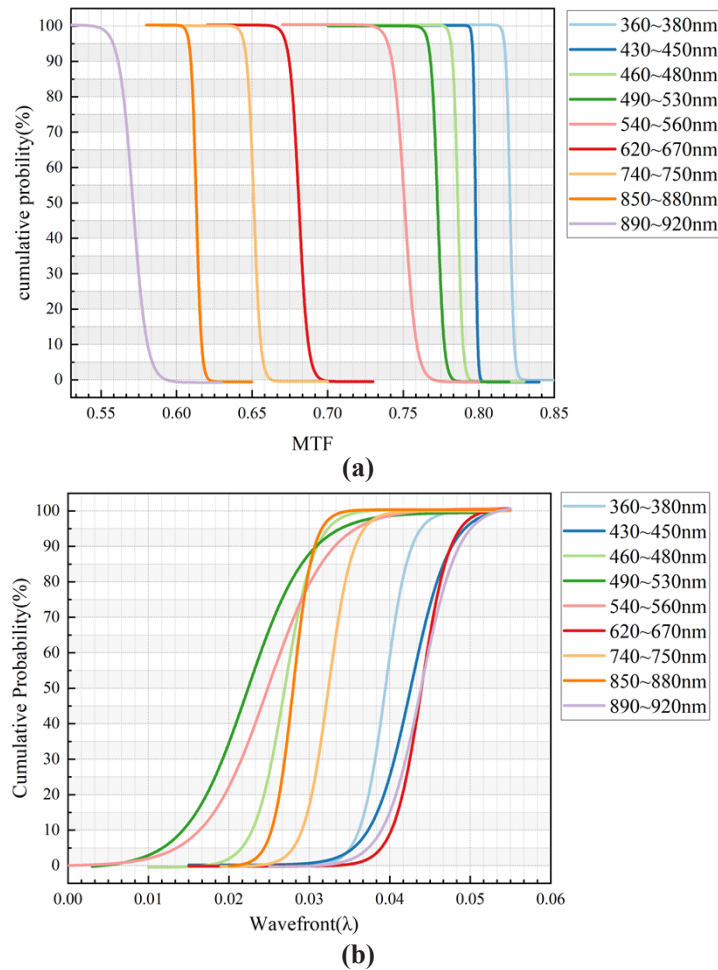
Fig. 10. (a) Cumulative probability curves of the MTF. (b) Cumulative probability curves of the RMS wavefront.

5. Stray radiation suppression

Stray light suppression is critical for high-resolution imaging. If stray light reaches the sensor, the image formed by an optical system will be degraded and may be submerged, causing the camera to malfunction. Since the Sun will inevitably appear in the FOV of the system when observing the Earth, the EAMC is designed to operate when the solar off-axis angle is greater than 45°, synchronous with the radiometer at the L1 point, which means that the solar radiation outside the 45° should be eliminated. The ability to obtain global Earth information within hours at the L1 point will allow sufficient Earth imagery and ERB data to be collected when observations begin at the 45° off-axis angle. This avoids making the instrument bulky and difficult to deploy by requiring complex shading structures for stray light suppression at smaller solar off-axis angles. Meanwhile, the Moon, cold space, and internal calibration sources will be observed during the Non-Earth imaging period. The stray light is suppressed and quantitatively analyzed in this section. Image quality is acceptable when stray light is 0.05% of the observed radiation. The point source transmission is applied to assess the influence of stray light on the optical system,

which is the ratio of stray illuminance generated on the detector to the illuminance of the entrance pupil [27].

5.1. Stray radiation suppression requirement

Considering the Sun as a 5900 K blackbody [28], the solar radiation in the spectral range of the EAMC $M_{sun}(\lambda_1,\lambda_2)$ is given by:

$$M_{sun}(\lambda_1, \lambda_2) = \int_{\lambda_1}^{\lambda_2} \frac{c_1}{\lambda^5[\exp(c_2/\lambda T_{sun}) - 1]} d\lambda \tag{11}$$

where λ_1 and λ_2 are each spectral channel's minimum and maximum wavelengths, respectively, and C_1, C_2 are the blackbody radiation constants; $C_1=3.7417749 \times 10^{-16}$ mK, $C_2=1.438769 \times 10^{-2}$ mK.

The solar irradiance at the entrance pupil of the EAMC $E_{ep}(\theta)$ can be written as:

$$E_{ep}(\theta) = \frac{R^2 M_{sun}}{l^2} \cos \theta \tag{12}$$

where R_{sun} is the radius of the Sun, $R_{sun} = 6.9599 \times 10^8$ m; θ is the angle between the Sun and the optical axis, and l is the distance between the optical system and the Sun, approximately the distance between the Sun and the Earth ($l= 1.496 \times 10^{11}$ m).

The solar irradiance reflected by the Earth E_{earth} in the spectral range of the EAMC can be described as:

$$E_{earth} = \alpha M_{sun} \sin^2 \beta \tag{13}$$

where α is the bond spectral albedo, as shown in Table 5 [29,30], and β is the view angle of the Sun to the Earth, $\beta = 16'$.

Table 5. Albedo specifications for calculating the RSR of the Earth at different wavelengths.[a]

Wavelength (nm)	360-380	430-450	460-480	490-530	540-560	620-670	740-750	850-880	890-920
Albedo	0.38	0.35	0.26	0.27	0.24	0.28	0.15	0.18	0.07

[a]Albedo specifications are the hemispheric annual average spectral reflectance as measured by SCIAMACHY over the period 2003-2010 [29,30].

The detector irradiance of each spectral channel E_d is given by:

$$E_d = \frac{\tau_o E_{earth}}{4F - number^2} \tag{14}$$

where τ_o is the optical system's transmittance, estimated at 0.85.

The PST of the system should satisfy Eq. (15):

$$PST(\theta) \leq 0.05\% \times \frac{E_d}{E_{ep}(\theta)} \tag{15}$$

5.2. Stray radiation suppression and simulation

The EAMC combines the aperture, field diaphragms, and an external baffle to suppress the stray light while blocking the non-utilized light from the primary system, as shown in Fig. 11(a). The external baffle's length and light inlet radius are 327 mm and 167 mm, respectively, which are determined using Eq. (16)–(17). There are twelve vanes inside the baffle that create the light traps. Based on the geometrography method [31] of vanes, the intersection of the light

reflected by the front stage vane and the FOV can be used to determine the height and position of the following stage vane. With the entrance pupil as the boundary, light entering the optical system from outside the FOV is reflected at least twice. The nine aperture and field diaphragms, determined by the direction and diameter of the light beam in each channel, are machined on a single component and placed in front of the sensor, with all nine field diaphragms set to 9 mm diameter and 4 mm thickness, and the aperture diaphragms set to 4 mm thickness and 25 mm diameter. A few threads are made on the inner wall of the lens barrel between the primary system and the subsystems, and all surfaces of the diaphragms and structural components are painted black to absorb the stray light.

$$D_s = D_e + 2L_s \tan \omega_E \tag{16}$$

$$D_e + L_s \tan \omega_E = L_s \tan \theta \tag{17}$$

where D_s and D_e are the diameters of the baffle and the primary system, respectively, and L_s is the length of the baffle.
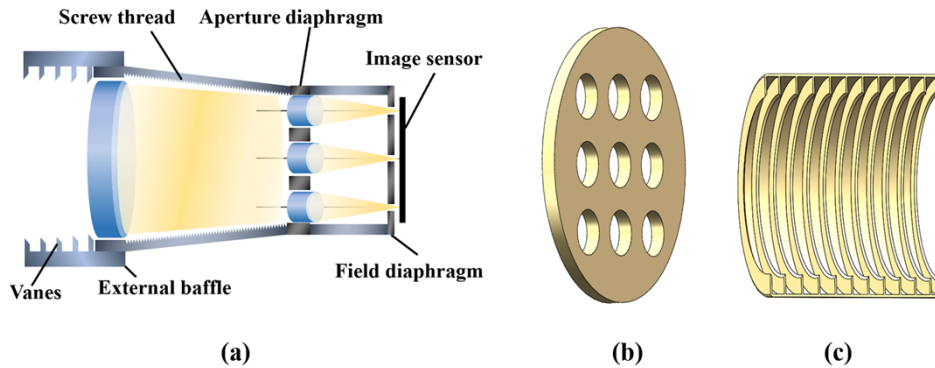
Fig. 11. (a) Schematic diagram of the primary structures for stray light suppression. (b) Field diaphragm structure schematic. (c) External baffle structure schematic.

The Monte Carlo method is adopted for the stray radiation simulation in TracePro. By setting up a circular light source containing 6.1 million rays with different spectral ranges and adjusting the angle between the normal vector of the light source and the optical axis, incident solar radiation from different directions can be simulated. Defining the surface parameters of the optical component materials and optomechanical structures is necessary to describe the scattering characteristics. Table 6 shows the optical properties of the surfaces in the simulation. Zemax supplies the lens size and material properties in the EAMC, and the matte black coating is called NEXTEL Velvet Coating 811-21, whose absorptivity and diffusivity are given in the manufacturer's official report [32,33]. The optical properties of the other surfaces are actual measurements taken by Lambda Research Corporation [34]. Narrowband filters are customized to an optical density (OD) of OD 6. The simulation threshold value is 10^{-9}, i.e., the trace stops when the energy of each randomly scattered ray decays to 10^{-9} times the original power.

The PSTs were determined by Monte Carlo simulation at 5° intervals from 5° to 75°, and the theoretical and simulated curves of the nine channels were plotted as shown in Fig. 12. The stray radiation suppression requirements are distinct depending on the Earth's RSR differing energy distribution and albedo in the nine wavelengths. It can be concluded from these plots that the PST curves of the nine channels are not exactly identical due to slightly different transmission paths of the scattered light, but their magnitudes and trends of change are consistent. There is a decrease in the PST curves as the off-axis angle increases and a sharp reduction within 20°. The stray light outside 40° can be suppressed to 0.05% of the target radiation, which reaches the order of 10^{-7} and exceeds the requirements. The simulation results show that the camera has

Table 6. Surface property sections for stray light simulation.

Surface type	Transmittance	Absorptance	Specular reflectance	BRDF[a]
Lens	0.9	0.02	0.03	0.05
Filter	0.85	0.1	0.02	0.03
Image sensor	0	1	0	0
Mechanical structure surface	0	0.9	0.05	0.05

[a]The Bidirectional Reflectance Distribution Function (BRDF) in this table defines the surface scattering characteristics.

good solar radiation suppression ability, and the stray light structure design is effective, which can meet the application conditions.
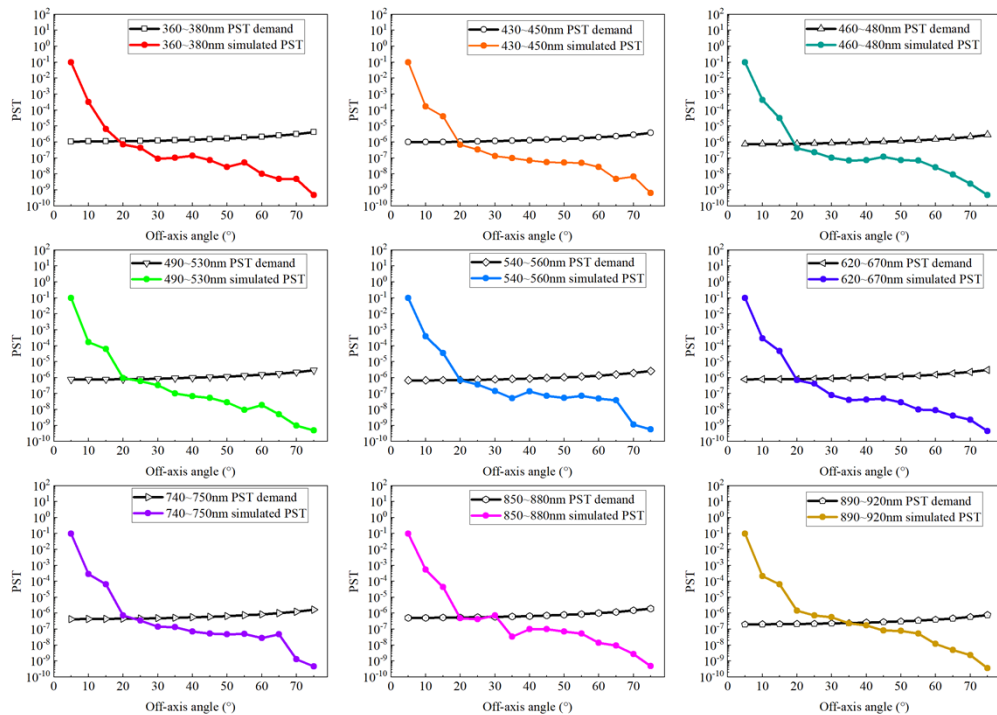
Fig. 12. PST comparison between design and theoretical requirements of the EAMC (interval of 5°).

The internal stray light suppression of the EAMC was also verified. After normalizing the spectral Earth-radiated power of the EAMC calculated in Section 5.1, an imaging beam incident of 2.5° FOV is set in TracePro. The normalized irradiance maps and profile curves before and after adding the stray light suppression structures are obtained from TracePro and are shown in Fig. 13. From Fig. 13(a), it is evident that before adding the structures, the observed signal on the detector is drowned out by the scattered and unused light from the primary system. The internal stray light has obvious spatial distribution features: The imaging rays form the central bright spots, and the unused rays directly illuminate the detector surface, while the darker ring is mainly composed of scattered light. The structures were then added, the simulation was rerun, and the results are shown in Fig. 13(b). As the apertures are precision machined, they can successfully block non-imaging rays. All internal structures are coated with a 0.9 full-spectrum absorptivity black paint, effectively absorbing scattered light and unwanted rays from the primary system. The

graphs show that only imaging rays are focused on the detector and that the integrated spectral irradiance of other regions is less than 2.34×10^{-5} from TracePro, which is about 0.031% of the detection irradiance and means that the internal stray light is well eliminated.
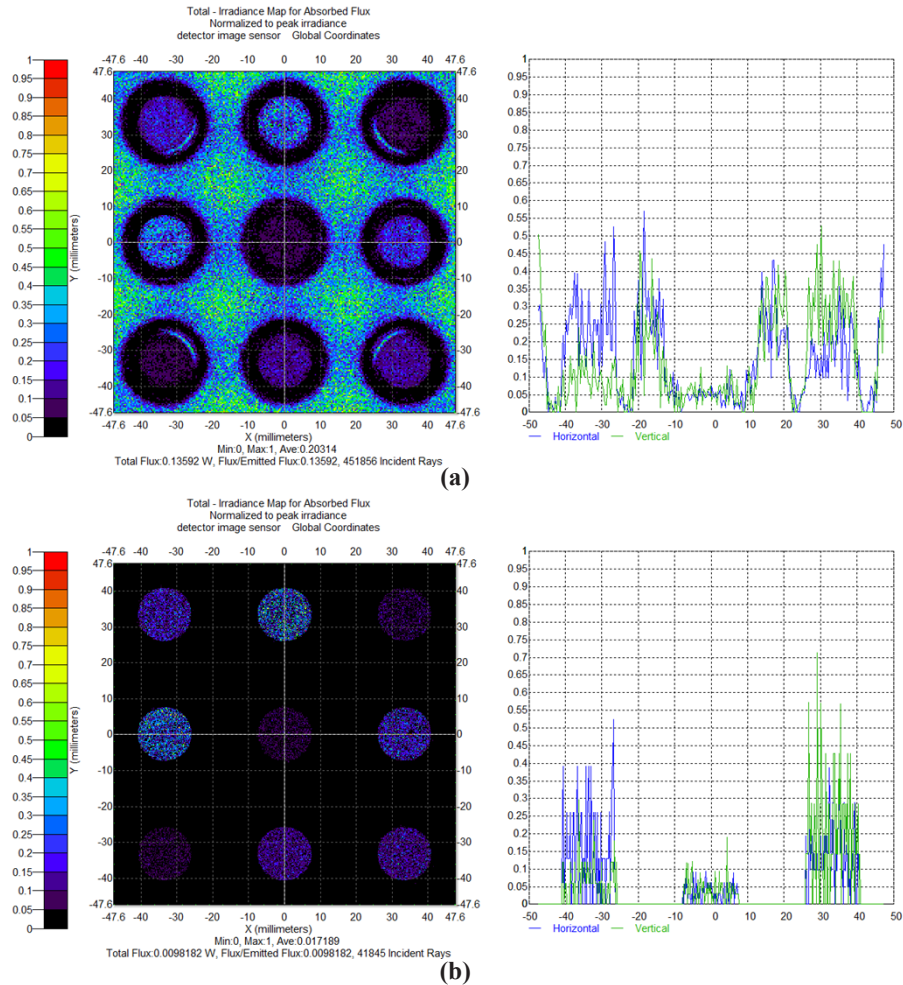
Fig. 13. (a) Normalized image irradiance map and profile corve without stray light suppression structures. (b) Normalized image irradiance map and profile curve with stray light suppression structures. The profile curves, with green lines representing the horizontal direction and blue lines representing the vertical direction, are centered on channels 360-380 nm.

6. Discussions

This paper proposes an aperture division multispectral camera with nine spectral channels: 360-380 nm, 430-450 nm, 460-480 nm, 490-530 nm, 540-560 nm, 620-670 nm, 740-750 nm, 850-880 nm, and 890-920 nm for scene identification. The EAMC can simultaneously obtain two-dimensional morphological and spectral information about the Earth. This will help to improve the real-time performance of the Earth's radiation measurements, enable accurate quantification of the ERF, and establish a pixel-based ADM.

The EAMC is designed with a full 2.5° FOV for limb-to-limb Earth observation. Our optical design indicates that the EAMC has sufficient image quality for scene identification with a spatial resolution of 10 km per channel, achieved with an RMS spot radius smaller than 9 μm across the FOV. The MTF values for all nine channels at 55 cycles/mm are ≥ 0.57, and the maximum wavefront PV value is 0.18λ, meeting the Rayleigh criteria and ensuring high-resolution imaging. The image distortion is almost negligible, with a maximum distortion of 0.1137%. The footprint diagram shows that the nine spectral images of the EAMC can be captured synchronously on a single 95.04 mm × 95.04 mm sensor. Tolerance analysis is critical in the next phase of EAMC prototyping and co-testing with the radiometer. Achievable lens tolerances are given for nine-channel MTFs above 0.5 and RMS wavefront values below 0.06λ with a cumulative probability of 97%, resulting from repeated tolerance tightening through sensitivity and Monte Carlo analysis of 1000 lens groups. Solar radiation can cause intense stray light, which is problematic for EAMC operation, so the requirements for stray light suppression have been analyzed. The aperture stop, the field stop, and the external baffle are used to suppress the stray radiation. The Monte Carlo simulations show that all nine-channel PSTs beyond 40° reach the order of 10^{-7}, which exceeds the requirements for fully simultaneous observation with the radiometer beyond the 45° off-axis angle. This allows the EAMC to operate in sync with the core radiometer and to be combined with the radiometer's data for climate research. Irradiance diagrams before and after adding the stray light extinction structures show good suppression of scattered and unused light to 0.031% of the detection signal. However, it should be noted that the aperture and field diaphragms require rigorous and precise machining to avoid incomplete occlusion of stray light, and the filters must be customized with an optical density of OD 6 to ensure the elimination of internal stray light.

7.   Conclusions

ERB monitoring at Earth-Moon L1 has been proposed, which can directly obtain integrated Earth radiation and avoid fitting errors in different time series observations. Nevertheless, the radiometer data cannot be used to characterize the radiative equilibrium effect of the ERF in various spectral bands, nor can the ADM be obtained, which is required for the retrieval of regional radiation. In this context, a multispectral camera that can provide regional Earth's RSR with a spatial resolution of 10 km for quantifying ERFs and constructing pixel-scale ADM is proposed in this manuscript.

The EAMC optical system, based on the principle of aperture division imaging, consists of 9 subsystems sharing a primary system for simultaneous multispectral imaging of the Earth has been successfully designed and analyzed. The satisfactory optical performance is confirmed by the results that the MTFs of all the spectral channels of the EAMC are greater than or equal to 0.57 at the Nyquist frequency of 55 cycles/mm, and the maximum wavefront PV value of 0.18λ complies with the Rayleigh criterion. The footprint diagram demonstrates the capacity to receive nine high-quality spectral images on one detector. Tolerance analyses show that the camera has adequate MTF and RMS wavefront values for attainable machine conditions. The stray solar radiation is suppressed by combining aperture, field diaphragms, and an external baffle. The Monte Carlo stray light analyses indicate that the internal stray is effectively eliminated, and the PST can reach the order of 10^{-7} for an off-axis angle of 40°, which meets the requirements and allows co-observation with the radiometer. The next steps will include the realization of the laboratory prototype, the co-testing with the radiometer, and the establishment of an experimental ADM based on the ground test data. Future work will focus on vacuum radiometric calibration and nine-channel cross-calibration.

Disclosures. The authors declare no conflicts of interest.

Data availability. Data underlying the results presented in this paper are not publicly available at this time but may be obtained from the authors upon reasonable request.

References

1. G. L. Stephens, G. G. Campbell, and T. H. V. Haar, "Earth radiation budgets," J. Geophys. Res. **86**(C10), 9739–9760 (1981).
2. P. Pilewskie, M. Hakuba, and G. Stephens, "The future of earth radiation budget observations beyond CERES: Libera and continuity of the ERB climate data record," in *EGU General Assembly* (2023).
3. L. Schifano, L. Smeesters, and F. Berghmans, *et al.*, "Optical system design of a wide field-of-view camera for the characterization of earth's reflected solar radiation," Remote Sens. **12**(16), 2556 (2020).
4. P. García-Palacios and J. Chen, "Emerging relationships among soil microbes, carbon dynamics and climate change," Funct. Ecol. **36**(6), 1332–1337 (2022).
5. M. D. Zelinka, S. A. Klein, and Y. Qin, *et al.*, "Evaluating climate models' cloud feedbacks against expert judgment," J. Geophys. Res. **127**(2), e2021JD035198 (2022).
6. D. Wu, W. Fang, and K. Wang, *et al.*, "Spaceborne relative radiometer: instrument design and pre-flight test," Remote Sens. **15**(12), 3085 (2023).
7. X. Ye, X. Yi, and C. Lin, *et al.*, "Instrument development: chinese radiometric benchmark of reflected solar band based on space cryogenic absolute radiometer," Remote Sens. **12**(17), 2856 (2020).
8. C. J. Smith, R. J. Kramer, and G. Myhre, *et al.*, "Effective radiative forcing and adjustments in CMIP6 models," Atmos. Chem. Phys. **20**(16), 9591–9618 (2020).
9. P. Arias, N. Bellouin, and E. Coppola, *et al.*, "Climate Change 2021: the physical science basis. Contribution of Working Group I to the Sixth Assessment Report of the Intergovernmental Panel on Climate Change," in *The Intergovernmental Panel on Climate Change AR6* (2021).
10. W. Su, J. Corbett, and Z. Eitzen, *et al.*, "Next-generation angular distribution models for top-of-atmosphere radiative flux calculation from CERES instruments: methodology," Atmos. Meas. Tech. **8**(2), 611–632 (2015).
11. B. A. Wielicki, B. R. Barkstrom, and E. F. Harrison, *et al.*, "Clouds and the Earth's radiant energy system (CERES): An earth observing system experiment," Bull. Am. Meteorol. Soc. **77**(5), 853–868 (1996).
12. N. G. Loeb, W. Sun, and W. F. Miller, *et al.*, "Fusion of CERES, MISR, and MODIS measurements for top-of-atmosphere radiative flux validation," J. Geophys. Res. **111**(D18), D18209 (2006).
13. N. G. Loeb, N. Manalo-Smith, and S. Kato, *et al.*, "Angular distribution models for top-of-atmosphere radiative flux estimation from the clouds and the earth's radiant energy system instrument on the tropical rainfall measuring mission satellite. part I: methodology," J. Appl. Meteorol. **42**(2), 240–265 (2003).
14. H. Zhang, X. Ye, and P. Zhu, *et al.*, "Observation system design and analysis for a new staring Earth radiation budget radiometer based on the Lagrange L1 point of the Earth–Moon system," Remote Sens. **14**(7), 1596 (2022).
15. T. Skauli, H. E. Torkildsen, and S. Nicolas, *et al.*, "Compact camera for multispectral and conventional imaging based on patterned filters," Appl. Optics **53**(13), C64–C71 (2014).
16. M. Yamaguchi, T. Teraji, and K. Ohsawa, *et al.*, "Color image reproduction based on multispectral and multiprimary imaging: experimental evaluation," in *Color Imaging: Device-Independent Color, Color Hardcopy, and Applications VII* (SPIE, 2001), pp. 15–26.
17. M. Hubold, E. Montag, and R. Berlich, *et al.*, "Multi-aperture system approach for snapshot multispectral imaging applications," Opt. Express **29**(5), 7361–7378 (2021).
18. K. Shinoda, Y. Ohtera, and M. Hasegawa, "Snapshot multispectral polarization imaging using a photonic crystal filter array," Opt. Express **26**(12), 15948–15961 (2018).
19. S. A. Ackerman, R. E. Holz, and R. Frey, *et al.*, "Cloud detection with MODIS. Part II: validation," J. Atmos. Ocean. Technol. **25**(7), 1073–1086 (2008).
20. D. Zhang, J. Shao, and X. Li, *et al.*, "Remote sensing image super-resolution via mixed high-order attention network," IEEE Trans. Geosci. Remote Sens. **59**(6), 5183–5196 (2021).
21. P. Wang, B. Bayram, and E. Sertel, "A comprehensive review on deep learning based remote sensing image super-resolution methods," Earth-Sci. Rev. **232**, 104110 (2022).
22. ANDANTA GmbH, "Optoelectronic image sensors for scientific applications," https://www.andanta.de/en/e-si-ccd.html.
23. O. K. Ersoy, *Diffraction, Fourier Optics and Imaging* (John Wiley & Sons, 2006).
24. Y. Li, "Research on compact division-aperture snapshot spectral imaging system," Doctoral dissertation, Xi 'an Institute of Optics and Fine Mechanics, University of Chinese Academy of Sciences (2018).
25. D. X. Zeng and X. P. Du, "Influence of detector's pixel size on performance of optical detection system," Chin. Space Sci. Technol. **58**(18), 6459–6479 (2013).
26. J.-M. Vigoureux and D. Courjon, "Detection of nonradiative fields in light of the Heisenberg uncertainty principle and the Rayleigh criterion," Appl. Opt. **31**(16), 3170–3177 (1992).
27. M. Asadnezhad, A. Eslamimajd, and H. Hajghassem, "Optical system design of star sensor and stray light analysis," J. Eur. Opt. Soc. Rapid Publ. **14**(1), 1–11 (2018).
28. E. Fest, *Stray Light Analysis and Control* (SPIE Press, 2013).
29. G. L. Stephens, D. O'Brien, and P. J. Webster, *et al.*, "The albedo of Earth," Rev. Geophys. **53**(1), 141–163 (2015).

30. A. Voigt, B. Stevens, and J. Bader, *et al.*, "The observed hemispheric symmetry in reflected shortwave irradiance," J. Clim. **26**(2), 468–477 (2013).
31. M. Wang, Z. Wang, and J. Bai, "Stray light analysis for hyper-spectral imaging spectrometer," Infrared Laser Eng. **41**(6), 1532–1537 (2012).
32. J. Lohrengel and R. Todtenhaupt, "Thermal conductivity, total emissivity and spectral emissivities of the Nextel Velvet 811-21 coating (RAL 900 15 deep black matted); Waermeleitfaehigkeit, Gesamtemissionsgrade und spektrale Emissionsgrade der Beschichtung Nextel-Velvet-Coating 811-21 (RAL 900 15 tiefschwarz matt)," PTB **106**(4), 259–265 (1996).
33. NEXTEL, "Decorative Coating for Matt Surfaces" https://www.nextel-coating.com.
34. T. R. Li, J. F. Wang, and X. M. Zhang, *et al.*, "Stray light analysis of the Xinglong 2.16-m telescope," Res. Astron. Astrophys. **20**(3), 30 (2020).